Influences of Nononshore Winds on Significant Wave Height Estimations Using Coastal X-Band Radar Images

Li-Chung Wu, Dong-Jiing Doong, and Jian-Wu Lai

***Abstract*— Marine X-band radar has been suggested to be capable of monitoring significant wave heights in both offshore and open sea areas. In contrast to studies on offshore radar, significant wave height estimations from coastal radar images, which exhibit complicated radar backscattering features, have received little attention. This study proposes a method for retrieving the significant wave height from coastal areas that are often influenced by nononshore winds. The square root of the signal-to-noise ratio in radar images has been widely applied to estimate the significant wave height. However, nononshore wind cases show a poor correlation between the square root of the signal-to-noise ratio and the *in situ* significant wave height. In addition, the spectral shapes from radar images in nononshore wind cases are very different from those in onshore wind cases. To improve the significant wave height estimations from coastal radar images, we implement an artificial neural network algorithm. After training and testing the algorithm, we confirm that the estimated significant wave heights are more reliable for both onshore and nononshore wind cases if the square root of the signal-to-noise ratio, power from nearshore radar subimages, and *in situ* wind components are included in the input layer of the neural network.**

***Index Terms*— Noncoherent X-band radar, nononshore winds, significant wave height.**

I. Introduction

WIND-GENERATED gravity waves are among the most significant ocean phenomena. The wave height, which can represent the power of waves, has received considerable attention in many fields of application. To obtain wave height data, *in situ* wave measurements are most often implemented. However, while *in situ* instruments are used to reconstruct the temporal variations in waves at a single point, remote sensing techniques provide information over broad areas, and research has confirmed the practicability of obtaining wave height data using satellites and land-based high-frequency (HF) radar. Unlike HF radar and satellite measurements, which can monitor up to several hundred square kilometers or even almost global areas, the effective measuring area for ocean waves by the X-band radar is limited to dozens of square kilometers. Nevertheless, marine X-band radar, which is typically used to detect coastlines and obstacles on the sea surface, is currently one of the most widely used tools for ocean remote sensing.

Radar returns from the sea surface are the key to obtaining information regarding the ocean environment, such as ocean waves, sea surface currents, and bathymetry, using X-band radar [1]–[3]. Previous studies have revealed the mechanisms of radar backscattering from the sea surface. The Bragg wavelength of X-band radar is approximately 1.5 cm, and the Bragg wavelengths of less than 4 cm are the most sensitive to the wind speed and wind direction. In addition, the radar backscattering enhanced by ripples is modulated by wind sea waves and swells [4], [5]. As a result, wind wave and swell patterns can be presented on X-band radar images. However, radar measurements are possible only when a local wind field is present [6], [7]. In addition to the wind speed, the wind direction also influences the strength of radar echoes. Because of the short fetch during nononshore winds, wind-generated short-scale waves are diminished [8], which is unfavorable to resonant Bragg scattering. As a consequence, wind waves and swells cannot be imaged well by X-band radar under nononshore wind conditions.

On the basis of different theories of X-band radar backscattering and imaging mechanisms of ocean waves, various applications using low grazing angle backscatter have been proposed to observe the significant wave height (H_s). To date, more than ten algorithms have been developed to estimate H_s from noncoherent X-band radar [9]. Although these algorithms were developed by different principles, they can be classified into two categories according to whether precalibration between the radar results and ground truth is necessary. An algorithm based on precalibration often relies on the signal-to-noise ratio (S_{NR}) from the radar image and a linear regression algorithm [5], whereas other algorithms require the power spectral density or image intensities to calibrate H_s [9]–[11]. In addition to linear regression, the artificial neural network (ANN) algorithm has also been applied for the X-band radar image analysis. ANN is an information processing technique that was first used in the early 1990s

Manuscript received November 1, 2020; revised February 17, 2021 and April 7, 2021; accepted April 19, 2021. Date of publication May 17, 2021; date of current version December 29, 2021. This work was supported in part by the Ministry of Science and Technology of Taiwan under Grant MOST 107-2221-E-006-212 and Grant MOST 108-2923-E-006-007-MY4. *(Corresponding author: Li-Chung Wu.)*

Li-Chung Wu is with the Coastal Ocean Monitoring Center, National Cheng Kung University, Tainan 701401, Taiwan (e-mail: jack18@mail.ncku.edu.tw).

Dong-Jiing Doong is with the Department of Hydraulic and Ocean Engineering, National Cheng Kung University, Tainan 701401, Taiwan (e-mail: doong@mail.ncku.edu.tw).

Jian-Wu Lai is with the Marine Industry and Engineering Research Center, National Academy of Marine Research, Kaohsiung 806614, Taiwan (e-mail: laijw0915@gmail.com).

Digital Object Identifier 10.1109/TGRS.2021.3077903

and has been applied in a variety of fields [12]. H_s was successfully estimated from $\sqrt{S_{\mathrm{NR}}}$ of offshore radar images using ANN [13]. Because the precalibration step using additional reference sensors could be a tough task in practical applications, the estimation of H_s from radar images without the use of *in situ* wave gauges was proposed in recent years, based mostly on shadowing-based algorithms in which the radar echo intensity is unnecessary for calibration [14]–[17]. In addition to shadowing-based algorithms, the correlation between a raw radar image and the corresponding noncalibrated wave elevation image was also proposed to estimate the wave height without using an external reference [18]. However, having a poor radar echo intensity or low S_{NR} value is unfavorable for determining the shadowing area from radar images or for determining a reasonable correlation. In summary, for both precalibration and calibration-free algorithms, the strength of the radar echo from the analyzed sea surface images is highly important. All of these algorithms assume that the radar echo intensities or S_{NR} values from the sea surface are highly correlated with the sea state. However, the wave height and other environmental factors influence the radar echo intensity. For open sea areas in which most of the environmental factors are homogeneous, the relationship between the radar echo intensity and H_s can be simple. Therefore, a single parameter, such as the radar echo intensity or $\sqrt{S_{\mathrm{NR}}}$, extracted from offshore radar images can be very useful for estimating H_s by using linear regression [19].

Although the practicability of observing H_s using offshore X-band radar has been demonstrated, the poor echo intensity due to nononshore winds remains a challenge to estimating H_s accurately using $\sqrt{S_{\mathrm{NR}}}$ from coastal radar. In addition, the surface wave signal strength in X-band radar images depends strongly on the range and azimuth (the angle between the antenna look direction and peak wave direction) [20]. It is possible to determine upwind or upwave cases for offshore radar observations to estimate H_s based on the subimage from the sea area with the strongest radar returns. However, the coastal land area prohibits us from selecting this area for the analysis of subimages. In addition, a single wave direction from a single location is unable to represent the real wave features within coastal areas due to the spatial heterogeneity of coastal waves [21].

A few cases of inaccurate H_s estimations under nononshore winds have been proposed [22]. However, the H_s estimations under different wind speeds and wind directions using coastal radar still need to be confirmed carefully. This study attempted to explore this issue. We focus on the influences of nononshore winds on H_s estimations using coastal radar images. Moreover, we discuss the feasibility of improving the H_s estimation if *in situ* wind components or other parameters are included within the algorithm. Field radar images and simultaneous *in situ* meteorological and sea-state data will be studied as follows.

II. Data Source

Fig. 1 shows the sea area of our study site within the coastal area of Hualien, Taiwan. The land area of the study site is almost entirely mountainous terrain, and the shoreline

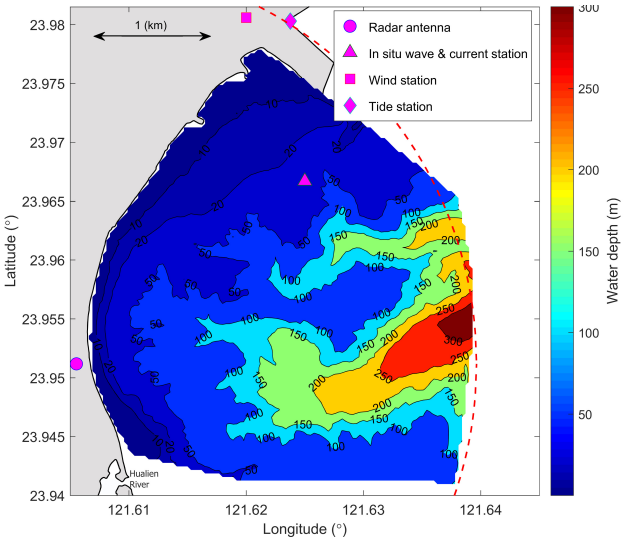

Fig. 1. Locations of different stations. The area where the radar echo intensities were recorded is delineated by a red dashed line. The land area is marked in gray. The different *in situ* stations are within 4 km of the radar antenna.

orientation is approximately 20°. To confirm the influences of environmental factors on radar backscattering, we collected *in situ* wind, wave, current, and tide data from adjacent stations. Wave data measured by a bottom-mounted wave station are used for comparison to confirm the H_s results estimated from the radar image sequences. The bottom-mounted reference wave and current station is equipped with both a pressure sensor and a vertical acoustic beam to measure the *in situ* significant wave height. The locations of the radar antenna and different *in situ* stations are marked in Fig. 1. Our X-band radar is horizontally polarized and equipped with an antenna 2 m in length that yields an image sequence sampling rate of 0.7 Hz. We collected radar images over a spatial range of 3750 m with a grid size of 7.5 m. The system stores the logarithmically amplified radar backscatter information at a 12-bit image depth. The radar measurements were collected in 128 continuous images from the first 183 s of each hour.

To discuss the environmental influences on the radar measurements, simultaneous *in situ* meteorological and sea-state data were collected and analyzed. According to an *in situ* current data analysis over a one-year period, 88% of near-surface ocean currents are below 0.3 m/s. In addition, most of the current directions are roughly parallel to the shoreline. The influence of the radar echo intensity due to wave-current interactions is not obvious.

In general, the influences of tides on the radar measurements in coastal areas should not be ignored. In coastal areas with high tidal differences and mild topography, low tides may result in a large area of shallow water, in which waves become steep and even break. Steep and breaking waves increase the strength of radar backscattering and, consequently, influence the H_s estimation using noncoherent radar. The mean tidal range in the study site is 1.2 m, and the nearshore slope, which is defined as the ratio of the closure depth over the horizontal distance between the closure depth and the

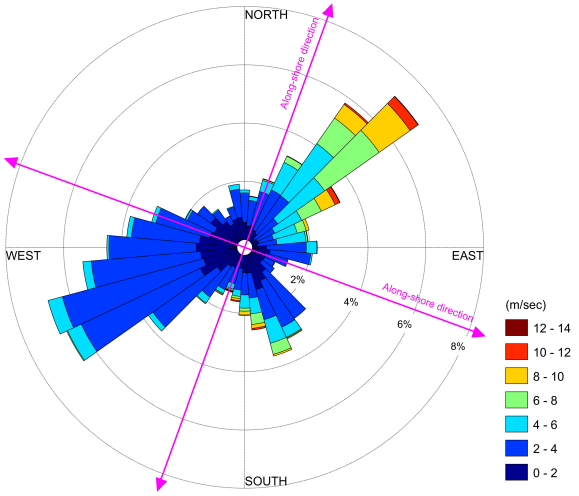

Fig. 2. Wind rose diagram. The difference in the wind strength between onshore and nononshore winds is obvious.

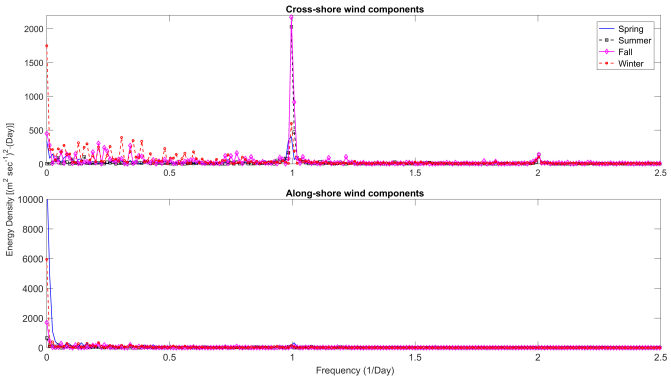

Fig. 3. Spectra of the cross- and along-shore wind components. There is an apparent one-day oscillation of the cross-shore winds. In contrast, there are almost no diurnal variations in the along-shore winds.

shoreline, is 0.13. According to the conditions of this tidal range and the nearshore slope, the horizontal distance between high-tide and low-tide shorelines is approximately 10 m. The pixel spacing of our radar image is 7.5 m, which means that the horizontal distance between the high-tide and low-tide shorelines is within 2 pixels on the radar images. Under this condition, the influence of tides on the nearshore radar backscattering is not obvious. Rainfall also has a significant impact on radar signals backscattered from the ocean. In the presence of rain, the radar backscatter intensity is enhanced. However, wave signatures are eliminated due to the noise introduced by rain [23]. Therefore, we manually check all the radar images to find and remove the radar cases recorded during rain. Noise from rain influenced 8% of our radar cases; thus, our radar dataset influenced by noise due to different rainfall intensities is insufficient. Consequently, the influence of rain-induced noise on H_s estimations using X-band radar is not discussed in this study.

In summary, this sea area is a suitable site to focus on the influences of nononshore winds on H_s estimations using noncoherent radar. We collected data over a period of approximately one year using different measurements. After removing the data impacted by rain and the data lacking simultaneous *in situ* data, there were approximately 3200 cases with simultaneous radar and *in situ* data.

III. Wind Features in the Study Site

The wind is one of the most significant factors inducing radar sea returns [24]. Fig. 2 shows that the stronger winds in the study area originate mainly from the northeast and adjacent directions. These strong winds are mainly due to the effects of winter monsoons, where few winds with very high speeds are due to the influence of typhoons.

In addition to the winter monsoons, we also observe interdiurnal wind variations. Unlike open sea areas, sea–land breezes are often unavoidable in coastal areas. The temperature difference between the land and the sea is a fundamental cause of these sea–land breezes. During the day, this temperature difference increases because of the difference between the hot land and cool sea, which produces a pressure difference at low levels in the atmosphere. This pressure difference disappears at night, and the temperature difference is sometimes reversed [25], which can cause winds from the land side to move in an offshore direction. In general, the strengths of nononshore winds are normally weaker than those of onshore winds and blow in roughly the opposite direction. Our study site faces the Pacific Ocean, which is the largest body of water in the world; the size of a water body has a great influence on the strength of the sea–land breeze. In addition, the study area includes a mountainous area; thus, mountain–plain winds are also unavoidable. In general, mountain–plain breezes blow from the plains toward the mountains during daytime and from the mountains toward the plains at night. Because the mountain–plain wind direction is similar to the direction of the sea–land breeze, nononshore winds are frequent.

To classify the wind cases, we decompose the *in situ* winds into cross-shore and along-shore wind components. A natural shoreline cannot be completely straight; thus, the wind direction and shoreline orientation relationships can be diverse. To simplify this issue, the shoreline orientation is simply defined as 20°. The positive cross-shore wind components are defined as onshore winds. The negative cross-shore wind components are defined as nononshore winds. Based on this classification, approximately 52% of our samples belong to nononshore cases.

After analyzing the spectra of the cross-shore wind components based on different seasons (see Fig. 3), we observe an obvious energy density at the diurnal band whose frequency is 1 (1/day). The peak frequencies from the spring, summer, and fall spectra are all within this diurnal band. We confirm that the diurnal variations of cross-shore winds occur more frequently in summer and fall. We also observe an obvious energy density in the very low-frequency bins in winter due to the continuous and strong winds under the influence of the winter monsoon. In contrast to the cross-shore winds, the spectra of the along-shore wind components in all seasons show a strong energy density in the very low-frequency bins. We scarcely observe the one-day oscillations of along-shore winds.

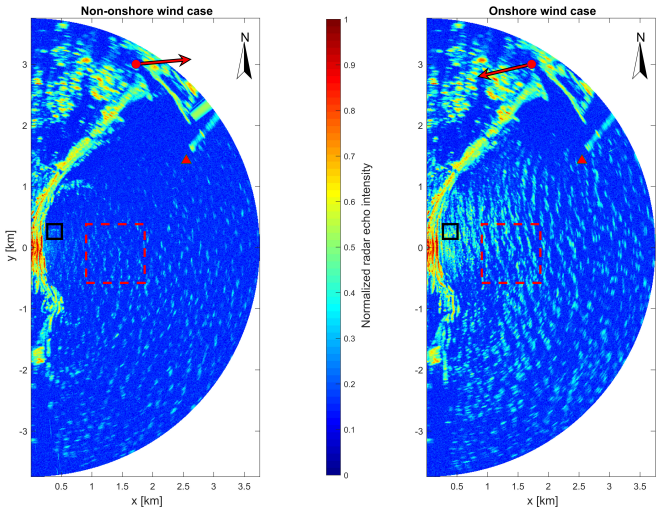

Fig. 4. Radar images of onshore and nononshore cases. The black square and red square on each image show the subimage areas to estimate P_n and $\sqrt{S_{\mathrm{NR}}}$, respectively. The wind directions of the onshore and nononshore wind cases are shown on the radar images as well.

TABLE I

ENVIRONMENTAL FEATURES OF TWO RADAR IMAGE CASES WITHIN 14 H

Observation time (UTC+8)		23 o'clock	12 o'clock
In situ meteorological and ocean wave features	Wind speed (m/sec)	4.1	4.2
	Wind direction (°)	265 (non-onshore)	77 (onshore)
	Significant wave height (m)	2.35	2.45
	Wave period (sec)	9.2	10.8
	Wave direction (°)	96	77
	Tidal height (m)	0.50	0.36
Radar echo features	$\sqrt{S_{NR}}$	0.37	2.36
	Nearshore power P_n	12.3	13.8

In general, the winds are influenced by different environmental factors, and nononshore winds are unavoidable at this study site. The backscatter from the sea in the horizontally polarized (HH) X-band radar cross section is maximized when the antenna looks in the wind direction and is minimized in the opposite direction [26]. This also results in poor radar sea returns when the wind direction is not onshore.

IV. INFLUENCES OF NONONSHORE WINDS ON SIGNIFICANT WAVE HEIGHT ESTIMATIONS

We have confirmed that the diurnal variations of cross-shore winds at our study site are obvious, especially in summer and fall. Fig. 4 shows the radar images of the nononshore wind and onshore wind cases that were recorded in the fall. These two images were recorded at 23 o'clock and at 12 o'clock on the next day. The time is based on the local time (UTC + 8). Because the western half-circles of the radar images at this study site represent the land area, we show only the eastern half-circle, which is mostly the sea area. The *in situ* meteorological and ocean wave features at these two hours

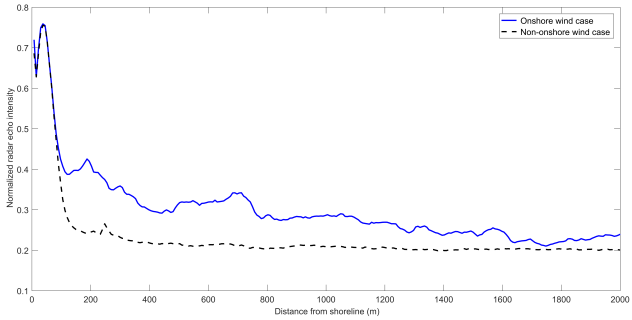

Fig. 5. Radar echo intensities in the cross-shore direction. For the nononshore case, the decay of radar echo intensities is limited only within the near range from the radar antenna.

are shown in Table I. The wave features, such as the *in situ* significant wave heights and directions, are similar at these 2 h. In general, the wind speed to induce ripples for the Bragg scattering should be faster than approximately 2∼3 m/s [27]. The wind speeds in these two cases are approximately 4 m/s. Although the wind speeds at these 2 h both belong to Beaufort number 3, their wind directions are almost opposite. For the sea area in the onshore wind case, we can identify the patterns of ocean waves that are key to estimating H_s using shadowing-based algorithms. Unlike the image of the onshore wind case, the radar echo intensities from the nononshore wind case are weak.

To compare the features of radar echo intensities from different radar image cases, we normalize the radar echo intensity from each image sequence as follows:

$$I_n(x, y, t) = I(x, y, t)/I_{\max} \tag{1}$$

where $I(x, y, t)$ is the recorded radar echo intensity from each case. In our study, the original analog radar video signal is digitized into 4096 gray levels. $I_n(x, y, t)$ is the normalized result from $I(x, y, t)$, and $I_{\max}$ is the maximal value of the entire $I(x, y, t)$ from all of our radar image cases. Due to the effects of the spatial inhomogeneity of the radar echo intensity, which is affected by the decay with distance and sea surface roughness, the radar sea returns can be diverse at different radar ranges. Fig. 5 shows the range series of normalized radar echo intensities in the cross-shore direction of two cases described in Table I. The patterns of sea surface waves or swells were eliminated by taking a time average of 128 continuous radar image sequences from each observation. Both the onshore and the nononshore wind cases show that the normalized radar echo intensities decay with distance from the shoreline. However, the difference between the radar echo intensities of these two cases is obvious at farther distances. For the nononshore case in Fig. 5, the decay of radar echo intensities is limited only within the near range from the radar antenna. Although the mechanics of radar returns from ocean waves are still not fully understood, specular reflection and Bragg backscattering are viewed as two of the most significant mechanics contributing to radar returns from the sea surface. Radar echoes are generated by the Bragg scattering at low grazing angles; at near-vertical grazing angles, radar echoes are generated by specular reflections from the sea

surface [28]. As the waves are close to the coast, the wave crests are roughly parallel to the shoreline, which is mainly due to wave refraction. The refracted waves are approximately perpendicular to the radar beam, and the front faces of these nearshore waves are conducive to specular reflections. In addition, microwave radiation is also reflected by the facets caused by nearshore breaking waves. The radar echo intensity due to specular reflections from large waves near the shoreline is more significant than that far from the shoreline. We select an area where the shortest distance between the shore and this area is only tens of meters, shown as the black square in each radar image of Fig. 4. To avoid the influence of land noise from the radar image, the size of the nearshore subimage is only 32×32 pixels. We estimate the power P_n from the nearshore subimage sequences. P_n is the integral of the 3-D spectral density from the small sea area subimage sequences. As shown in Table I, the P_n value from the onshore wind case is approximately 1.2 times that from the nononshore wind cases.

Compared to P_n, the parameter S_{NR} is more frequently applied for most of the H_s estimations from noncoherent X-band radar data. The definitions of S_{NR} are diverse according to different types of signals and different applications. For the issue of X-band radar, the S_{NR} value is determined by separating the different spectral components based on the wave dispersion relation, as follows [5], [19], [29]:

$$S_{\mathrm{NR}} = \int S_{\mathrm{W}}(\vec{\mathbf{k}})d^2k \Big/ \int S_{\mathrm{bgn}}(\vec{\mathbf{k}},\omega)d^2k d\omega \tag{2}$$

$$S_{\mathrm{W}}(\vec{\mathbf{k}}) = \int S_{\mathrm{W}}(\vec{\mathbf{k}},\omega)d\omega \tag{3}$$

where $\vec{\mathbf{k}}$ is the wavenumber vector, ω is the angular frequency, and $S_{\mathrm{W}}(\vec{\mathbf{k}},\omega)$ is the nonscaled wave spectrum, which can be estimated from the filtered spectrum $S_F(\vec{\mathbf{k}},\omega)$ as follows:

$$S_{\mathrm{W}}(\vec{\mathbf{k}},\omega) = S_F(\vec{\mathbf{k}},\omega)\cdot T_M(k) \tag{4}$$

$$T_M(k) \simeq k^{-\beta} \tag{5}$$

where $T_M(k)$ is the modulation transfer function. The value of β was empirically suggested to be 1.2. k is the wavenumber modulus. It should be noted that this empirical transfer function was determined using onboard marine radar in a deep water area (the water depth is approximately 600 m). Although the modulation transfer function was also investigated in a coastal area [30], the most suitable value of β is still under discussion. We still adopt $\beta = 1.2$, which is widely used in applications.

$S_{\mathrm{bgn}}(\vec{\mathbf{k}},\omega)$ in (2) is the spectral density of background noise, which can be estimated from $S_I(\vec{\mathbf{k}},\omega)$ as follows:

$$S_{\mathrm{bgn}}(\vec{\mathbf{k}},\omega) \simeq S_I(\vec{\mathbf{k}},\omega) - S_F(\vec{\mathbf{k}},\omega) - S_{\mathrm{HH}}(\vec{\mathbf{k}},\omega) \tag{6}$$

where $S_F(\vec{\mathbf{k}},\omega)$ is the spectral density estimation of the components located inside the wave dispersion shell, as follows:

$$\omega = (q+1)\sqrt{[g|\vec{\mathbf{k}}|/(q+1)]\tanh[|\vec{\mathbf{k}}|h/(q+1)]} + \vec{\mathbf{k}}\cdot\vec{\mathbf{U}} \tag{7}$$

where h is the water depth, $\vec{\mathbf{U}}$ is the surface current vector, and q is the order of the qth harmonic. In our study, we implement $q = 0$ and $q = 1$ to determine $S_F(\vec{\mathbf{k}},\omega)$ and $S_{\mathrm{HH}}(\vec{\mathbf{k}},\omega)$ from $S_I(\vec{\mathbf{k}},\omega)$, respectively. Because $\vec{\mathbf{U}}$ is often unknown, the least-squares method can be implemented to determine the wave dispersion shell within the image spectrum $S_I(\vec{\mathbf{k}},\omega)$ [31]. $S_I(\vec{\mathbf{k}},\omega)$ is the spectral density of the subimage sequences $I_n(x,y,t)$ using the discrete Fourier transform. The width of the dispersion shell is limited within the range of $\omega\left(\vec{\mathbf{k}}\right) \pm \Delta\omega$, where $\omega\left(\vec{\mathbf{k}}\right)$ is estimated using (7), and $\Delta\omega$ is the angular frequency step used to sample the spectra [29].

The spectral components are located within the spectral domain $\Omega_{\vec{k},\omega}$ defined as follows:

$$\Omega_{\vec{\mathbf{k}},\omega} \equiv [-k_{xc}, k_{xc}) \times \left[-k_{yc}, k_{yc}\right) \times [\omega_{th}, \omega_c) \tag{8}$$

where k_{xc}, k_{yc}, and ω_c are the Nyquist wavenumbers and angular frequency, which are limited by the spatial and temporal sampling resolutions of radar image sequences. ω_{th} is the frequency threshold to avoid the influences of static patterns and the group line from the image spectrum. We adopt $\omega_{th} = 2\pi \cdot 0.04$ rad/s based on [32].

At present, the influences of breaking waves on the values of $\sqrt{S_{\mathrm{NR}}}$ are still unclear. To select the suitable subimage area for the estimation of $\sqrt{S_{\mathrm{NR}}}$, we avoid the nearshore area, which is influenced by breaking waves. We focus on the area marked by a dashed rectangle in Fig. 4, which is approximately 1 km from the shoreline. The water depth in this area is over 40 m. The size of the subimage is the result of a tradeoff between the accuracy of the estimates and the homogeneity constraints on the sea parameters [33]. Although no final conclusion has yet been reached on the best size of the subimage, the side lengths of the subimage are often suggested to range from 64 to 256 pixels [7], [34], [35]. Because the inhomogeneity of the coastal wave patterns within 256 pixels is obvious in our study site, we select the subimage with the size of 128×128 pixels to estimate $\sqrt{S_{\mathrm{NR}}}$.

Table I also presents the $\sqrt{S_{\mathrm{NR}}}$ values estimated from the subimage of this sea area. The $\sqrt{S_{\mathrm{NR}}}$ value from the onshore wind case is approximately 6.4 times that from the nononshore wind case. Compared to the ratio of nearshore power P_n values in Table I, the ratio of $\sqrt{S_{\mathrm{NR}}}$ values between the onshore and nononshore wind cases is much larger. For the cases presented in Table I, $\sqrt{S_{\mathrm{NR}}}$ is sensitive to the influence of nononshore wind. This result preliminarily confirms that the wave signals from radar sea returns are sensitive to the coastal wind direction. In case we need to estimate H_s based on radar sea returns, the influences on nononshore winds cannot be ignored.

Table I presents only two cases. We continue to discuss this issue using all of our radar measurements. The values of $\sqrt{S_{\mathrm{NR}}}$ under different wind conditions are first explored. As shown in Fig. 6, the positive cross-shore and positive along-shore wind components are slightly correlated with $\sqrt{S_{\mathrm{NR}}}$. Although most of the higher values of $\sqrt{S_{\mathrm{NR}}}$ are related to strong positive wind components, the correlation coefficient between $\sqrt{S_{\mathrm{NR}}}$ and the positive cross-shore wind speeds is only 0.6. The negative cross-shore wind components that blow from the land side show poorer correlation with

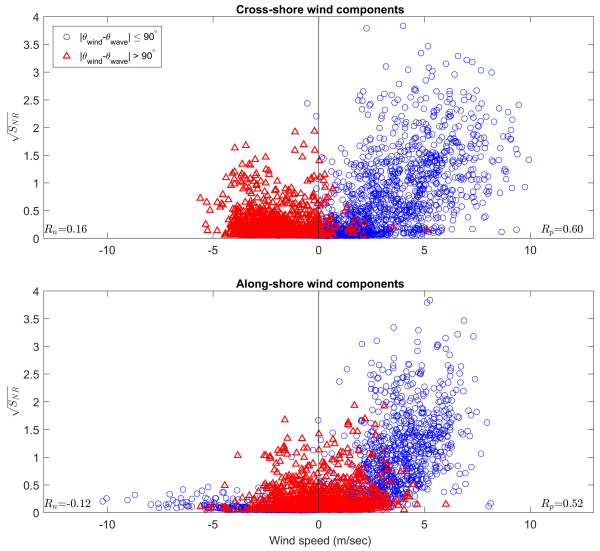

Fig. 6. Relationships between the *in situ* wind speed components and $\sqrt{S_{\mathrm{NR}}}$. Higher values of $\sqrt{S_{\mathrm{NR}}}$ occur when the wind and wave directions are similar. The correlation coefficients between $\sqrt{S_{\mathrm{NR}}}$ and the positive speed components (R_p), and the correlation coefficients between $\sqrt{S_{\mathrm{NR}}}$ and the negative speed components (R_n) are both shown.

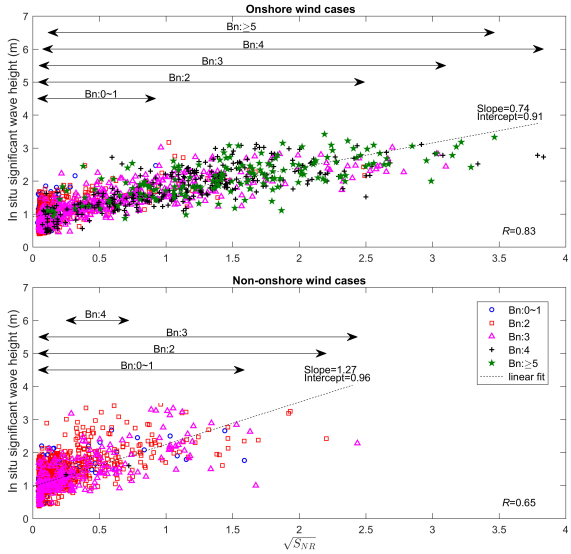

Fig. 7. Relationships between $\sqrt{S_{\mathrm{NR}}}$ and the *in situ* significant wave height in the onshore and nononshore wind cases. The ranges of $\sqrt{S_{\mathrm{NR}}}$ under different Beaufort scales of wind speed are also shown as the lines with double arrows. The correlation coefficient (R) between $\sqrt{S_{\mathrm{NR}}}$ and the *in situ* significant wave height is also shown in each plot.

$\sqrt{S_{\mathrm{NR}}}$, and the correlation coefficient is 0.16. Fig. 6 also shows the relationship between the wind directions (θ_{wind}) and wave directions (θ_{wave}). Because most of the coastal wave directions are more or less onshore, the obvious differences between the wind and wave directions often occur during the negative cross-shore wind cases. In addition to the negative cross-shore wind components, the along-shore wind components also show poor correlations between the wind speed and $\sqrt{S_{\mathrm{NR}}}$ if the wave direction is far from the wind direction.

The relationship between $\sqrt{S_{\mathrm{NR}}}$ and the *in situ* significant wave height in the open sea is linear and highly correlated with the measurements by offshore radar stations [19]. However, this relationship still needs to be verified in coastal areas. Fig. 7 shows the relationship between $\sqrt{S_{\mathrm{NR}}}$ and the *in situ* significant wave height in the coastal waters. To present the wind features effectively, our *in situ* wind speed data are classified according to the Beaufort scale (B_n). We observe that high $\sqrt{S_{\mathrm{NR}}}$ values are often related to high onshore wind speeds. On the other hand, weak onshore winds do not result in high $\sqrt{S_{\mathrm{NR}}}$ values. Unlike the onshore wind cases that include sufficient cases with strong wind speeds, the nononshore wind cases of the Beaufort number 4 compose only 0.5% of the whole nononshore wind dataset. Because the nononshore wind samples with high wind speeds are insufficient, the $\sqrt{S_{\mathrm{NR}}}$ relationships for the wind speed cases with Beaufort number 4 are limited within a narrow range of $\sqrt{S_{\mathrm{NR}}}$. For the nononshore wind cases, the correlation coefficient between the $\sqrt{S_{\mathrm{NR}}}$ values and *in situ* significant wave height is poor. We also fit our data using linear regression, which is widely applied to estimate the H_s using radar data. Fig. 7 shows that the intercepts for the onshore and nononshore wind cases are similar. However, the value of the slope from the nononshore wind cases is approximately 1.7 times that of the slope from the onshore wind cases. Compared to the onshore wind cases, the $\sqrt{S_{\mathrm{NR}}}$ values from nononshore wind cases are smaller. We also observe more nononshore wind cases with low values of $\sqrt{S_{\mathrm{NR}}}$ (<1) but large values of the *in situ* significant wave height (>2.5 m), which is why the slope of the linear fit from the nononshore wind cases was higher than that from the onshore wind cases. To accurately estimate H_s from $\sqrt{S_{\mathrm{NR}}}$, a high correlation between $\sqrt{S_{\mathrm{NR}}}$ and the *in situ* significant wave height is necessary. However, the nononshore wind cases show a poor correlation, which can result in an obvious underestimation of H_s using low $\sqrt{S_{\mathrm{NR}}}$.

We also discuss the relationships between P_n and the *in situ* significant wave height (see Fig. 8). Although both onshore and nononshore wind cases show positive correlations between P_n and the *in situ* significant wave height, the correlation coefficients (R) are poor. Because the area of the subimage is within the surf zone, the influence of breaking waves on the radar echo return is also unavoidable. Comparing the results of Figs. 7 and 8, the *in situ* significant wave heights show a higher correlation with $\sqrt{S_{\mathrm{NR}}}$ than with P_n. However, both onshore and nononshore wind cases show similar values of P_n under a higher *in situ* significant wave height, which means that higher values of P_n are often related to higher *in situ* significant wave heights, regardless of whether they are onshore wind cases or nononshore wind cases.

To estimate H_s accurately, a single parameter is not enough. In Section V, we will attempt to integrate the parameters of $\sqrt{S_{\mathrm{NR}}}$ and P_n to estimate H_s.

In addition to the features of $\sqrt{S_{\mathrm{NR}}}$ and P_n, we also explore the spectral features obtained from the radar images. The 1-D backscattering spectra of radar can be obtained based on the integral value of the nonscaled wave spectrum. We focus on the influences of nononshore winds on the spectral shape. The distributions of the spectra are diverse, and the spectral width parameters are applied here to quantify the spectral shapes as

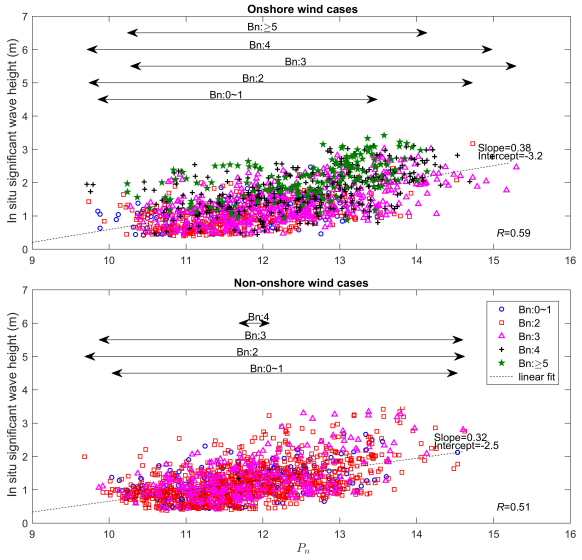

Fig. 8. Relationships between P_n and the *in situ* significant wave height in the onshore and nononshore wind cases. The ranges of P_n from the onshore and nononshore wind cases are similar. The correlation coefficient (R) between P_n and the *in situ* significant wave height is also shown in each plot.

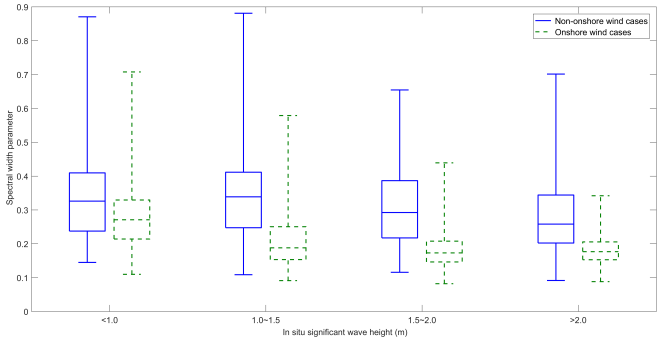

Fig. 9. Relationships between the *in situ* significant wave height and the spectral width parameter from radar images. Under similar sea states, the spectral widths are larger in the nononshore wind cases than in the onshore wind cases.

follows:

$$w_d = \sqrt{\frac{m_0 m_2}{m_1^2} - 1} \tag{9}$$

$$m_n = \int_0^\infty f^n S_w(f). \tag{10}$$

The spectral width parameter w_d has a value between 0 and 1, and it serves as an index of the narrowness of the spectral bandwidth; the spectrum is said to be narrow-banded when the values of these parameters are very small [36]. In addition, higher *in situ* significant wave heights are roughly related to smaller values of w_d [37]. Fig. 9 shows the relationship between the *in situ* significant wave height and the spectral width parameter w_d from the radar images. The onshore wind cases show that the values of w_d decrease, while the *in situ* significant wave heights increase. However, the nononshore wind cases show wider spectral shapes under similar *in situ* significant wave height conditions. Even though an empirical relationship is applied to correct the spectral shape, the spectral shape from the nononshore wind case is still unreliable. This is probably due to insufficient radar echoes from the sea surface during the occurrence of nononshore winds.

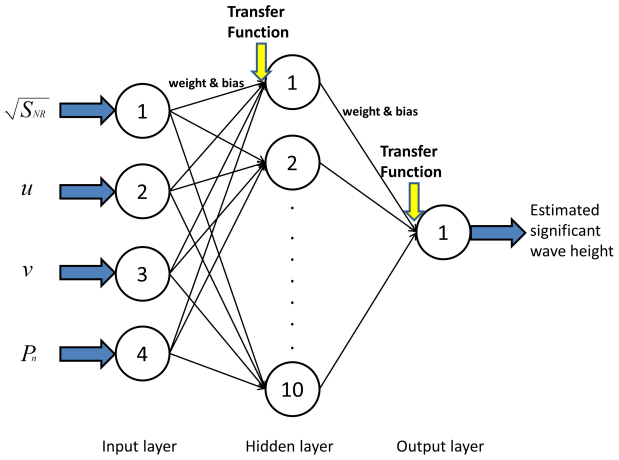

Fig. 10. ANN-based H_s estimator in this study. There are only ten neurons in the hidden layer of the ANN structure. $\sqrt{S_{\rm NR}}$, P_n, and zonal and meridional winds (u and v) are included as the ANN inputs.

The unreliable spectral shape from the nononshore cases is a factor affecting the accuracy of the estimated wave spectrum. The mean wave period, which can be estimated from the moments of the wave spectrum [38], must be influenced by the spectral width. Hence, the estimated H_s from the area of the wave spectrum cannot be accurate in the case where the spectral shape from the radar is far from that from real ocean waves.

V. Improvement of the Significant Wave Height Estimation Under the Influence of Nononshore Winds

After confirming the influence of nononshore winds on radar observations, we now focus on improving the H_s estimations. To estimate H_s accurately from the radar data, we cannot rely on only $\sqrt{S_{\rm NR}}$ or P_n individually. In addition, the relationship between the shoreline and wind direction is a key influencing factor on the values of $\sqrt{S_{\rm NR}}$ and P_n. We attempt to integrate these multiple factors to estimate H_s using the ANN algorithm. Although the ANN algorithm has been applied to wind and wave estimations from X-band radar images [13], [39], these radar images were observed from an offshore platform. Our study focuses on coastal areas in which the influences of nononshore winds and the inhomogeneity of wave patterns on radar returns must be considered. To estimate H_s using coastal radar images, multilayer perception (MLP) with a feedforward algorithm is implemented in our study. The ANN structure in our study is shown in Fig. 10. Our study focuses on the practicality of employing ANN to improve the H_s estimation from coastal radar images instead of optimizing the ANN structure. Hence, we implement only a simple structure for the ANN algorithm; there are no cycles or loops in the network.

To implement the ANN, all of the samples are classified into two parts. One part is for training, and the other is for testing. To confirm the feasibility of wave height estimation

TABLE II
DIFFERENT INPUTS FOR THE ANN ALGORITHM

Input parameters / Training case	$\sqrt{S_{NR}}$	P_n	u	v
Case (I)	No	No	Yes	Yes
Case (II)	Yes	No	No	No
Case (III)	No	Yes	No	No
Case (IV)	Yes	Yes	No	No
Case (V)	Yes	Yes	Yes	Yes

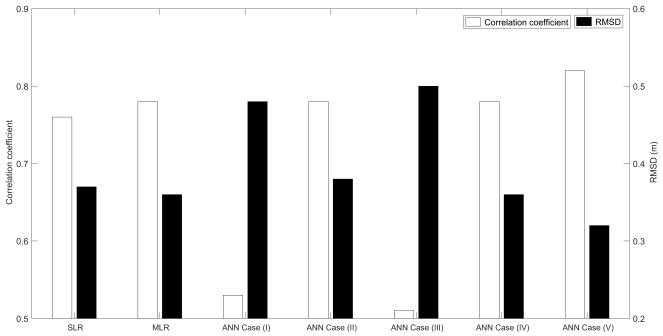

Fig. 11. Results of the H_s estimation using SLR, MLR, and the ANN algorithm. The testing results of Case (V), which integrates $\sqrt{S_{\rm NR}}$, P_n, and the wind components into the ANN structure, show the best H_s estimation results among all the tests.

using ANN, both training and testing datasets should include cases of higher sea states. The higher sea states in our study site are related to weather events, such as typhoons and monsoons. We split our data based on different weather events and integrate the odd events for training samples and the even events for testing samples.

To consider the influences of onshore and nononshore winds, the zonal wind (u) and meridional wind (v) components are also candidate input parameters for ANN training. As a result, the candidate input parameters for the training include $\sqrt{S_{\rm NR}}$, P_n, u, and v. To confirm the necessity of these parameters within the network, we design different cases. Table II shows the input parameters for the different training cases.

After implementing different cases, we can confirm the accuracies of the estimated H_s by using the testing results. Fig. 11 shows the testing results of the ANN based on different inputs. Both the ANN results and the H_s estimations using linear regression are presented in Fig. 11. Simple linear regression (SLR) and multiple linear regression (MLR) are both implemented to estimate the calibration constants here. A single input $\sqrt{S_{\rm NR}}$ is included within the SLR, while $\sqrt{S_{\rm NR}}$, P_n, and wind information are all included within the MLR to estimate the calibration constants. The correlation coefficient and the root mean square deviation (RMSD) are applied here to confirm the different results. Because of the influences of nononshore winds, we cannot obtain highly accurate estimates of H_s using SLR, and the MLR results show better performance than the SLR results. Compared to

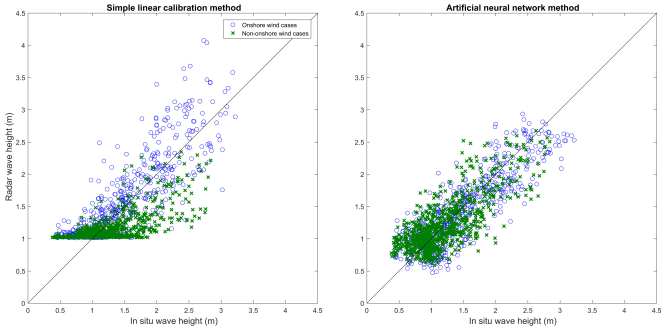

Fig. 12. Comparisons of the significant wave height estimations using different methods. Compared to the results using the simple linear calibration method, the accuracies of the significant wave height estimations under nononshore winds are obviously improved.

the SLR results, the results of Case (II) using ANN with a single input ($\sqrt{S_{\rm NR}}$) demonstrate similar performance.

For Case (I), we use only the wind data as the ANN input. We verify that the significant wave height estimations cannot be accurate when relying only on wind information (when $\sqrt{S_{\rm NR}}$ and P_n are excluded).

According to previous studies on this issue, $\sqrt{S_{\rm NR}}$ is widely regarded as the most important factor for accurately estimating H_s. The results of Cases (II) and (III), in which $\sqrt{S_{\rm NR}}$ and P_n are included, respectively, confirm that $\sqrt{S_{\rm NR}}$ is more effective than P_n at estimating H_s using the ANN algorithm. However, a single input is still not enough to train the algorithm. Fig. 11 further shows that the H_s estimations using ANN with more suitable parameters as inputs can be highly accurate. In other words, the H_s estimation using ANN can be significantly improved if $\sqrt{S_{\rm NR}}$, P_n, and the wind components are all included as inputs. Consequently, in a comparison between the H_s estimations using MLR and Case (V) using ANN, including $\sqrt{S_{\rm NR}}$, P_n, and wind information as inputs, the ANN model shows better performance. This is because our MLR model assumes that all the inputs are linearly correlated with the significant wave height; as shown in Fig. 8, the linear relationship between P_n and the *in situ* significant wave height is not clear. Moreover, according to various wave theories, the relationship between the significant wave height and wind speed is not simply linear [40]. In contrast to MLR, ANN training is an unconstrained nonlinear minimization problem in which the network is iteratively modified to minimize the overall mean or total squared error [41]. This is one reason that the H_s estimations from Case (V) using ANN can achieve better performance. Although the MLR algorithm can be designed to be more complicated and nonlinear, this issue is beyond of the scope of this study.

Fig. 12 shows scatter plots of the significant wave height estimations using SLR and ANN testing Case (V). H_s from the SLR estimations (approximately 1 m) shows obvious bias. As shown in the results in Fig. 7, the *in situ* significant wave height can range from 0.3 to 2 m, while the corresponding $\sqrt{S_{\rm NR}}$ values are less than 0.1. Thus, the H_s estimation using SLR can be uncertain if $\sqrt{S_{\rm NR}}$ is too weak. Fig. 7 also shows the intercepts of the regression lines in the onshore and nononshore cases (both approximately 1 m), which implies

that the H_s estimations using these linear relationships must be at least approximately 1 m. The value of $\sqrt{S_{\mathrm{NR}}}$ is strongly dependent on the analysis window range and azimuth from the radar images. Although better SLR results can be obtained by averaging $\sqrt{S_{\mathrm{NR}}}$ over all directions or by selecting a suitable range of analysis window locations [20], coastal areas with complicated shorelines limit us to this implementation. This is a reason that we observe obvious bias in the SLR results when the $\sqrt{S_{\mathrm{NR}}}$ values are not adequately high. In contrast, we can confirm that the H_s estimations under nononshore winds can be obviously improved if we integrate $\sqrt{S_{\mathrm{NR}}}$, P_n, and the wind components into the ANN structure.

Although our study focuses on the issue of radar monitoring under the influences of coastal winds, the influence of the changing tidal height on nearshore radar backscattering for sea areas with large tidal ranges and mild slopes of coastal topography should not be ignored. In the case of estimating the coastal significant wave height in a shallow water area, the tidal height should be an input parameter for the ANN training and testing processes.

VI. Conclusion

The significant wave height (H_s), which describes the sea state in a statistical sense, may be regarded as the most useful sea-state parameter in different maritime applications. The area of interest for the data required for coastal engineering, coastal area protection and management, and oceanic recreation is often within several kilometers of the shoreline. Hence, X-band radar could be a suitable monitoring tool to provide H_s information operationally. To date, most previous studies have confirmed the accuracy of H_s estimations using radars installed on open sea platforms. Compared with radars on open sea pile stations or ships, coastal land-based radar measurements are inexpensive and simple to operate. Accordingly, an increasing number of applications have acquired data based on nearshore X-band radar measurements. However, the issue of estimating H_s using coastal radar images has received little attention. One of the reasons for this limited attention is the complications and inhomogeneity of radar backscattering from the coastal sea surface. When focusing on coastal areas, the influences of terrestrial weather, such as land breezes on radar backscattering, cannot be ignored. Moreover, because of the influence of the coastal topography, the dominant wave direction is often roughly onshore. However, the wind direction can continuously change due to the effects of sea–land breezes. As a result, the wind and wave directions are sometimes opposite in coastal areas. In addition, wave transformation phenomena, such as wave refraction, shoaling, and breaking due to the influences of the coastal topography, are also important for the mechanism of radar backscattering. Although our study focuses on the issue of wave measurement, the applications of current and shallow water bathymetry measurements using X-band radar rely on clear wave patterns, which are also related to a stronger radar echo intensity or higher signal-to-noise ratio in sea surface images. Therefore, the influences of the coastal wind speed and wind direction on the radar measurements must be confirmed carefully.

Our study area is a microtidal coast, and the nearshore slope is steep. The wave transformations due to shallow water are limited within very small areas. As a result, we can focus on the coastal wind effects on radar monitoring. To confirm the feasibility of estimating H_s under the influences of different wind directions, our study collected coastal radar images and simultaneous *in situ* wind and wave data over a period of approximately one year. Due to the effects of sea–land breezes and mountain–plain breezes, the wind sometimes changes to the opposite direction within one day. To simplify the wind cases, the positive cross-shore wind components in our study site are defined as onshore winds, while the negative cross-shore wind components are defined as nononshore winds.

We observe obvious differences in the wave patterns in the sea surface images between the onshore and nononshore wind cases even when the other environmental conditions, such as the wind speed, tidal height, and wave conditions, were similar between the two cases. The most common method for estimating H_s is based on the square root of the signal-to-noise ratio ($\sqrt{S_{\mathrm{NR}}}$) using linear regression. H_s estimated from the radar signals of onshore wind cases is more accurate than that from the radar signals of nononshore wind cases. Some of the nononshore wind cases show low $\sqrt{S_{\mathrm{NR}}}$ values, while the *in situ* values of significant wave heights are large. This finding means that the estimated values of H_s are underestimated when the coastal radar images of some nononshore wind cases are used. We also check the results of the linear regression between the $\sqrt{S_{\mathrm{NR}}}$ values and *in situ* significant wave height. The slopes of the linear fit between the onshore and nononshore wind cases vary. When H_s must be estimated based on the linear fit between $\sqrt{S_{\mathrm{NR}}}$ and *in situ* H_s, we should implement the estimation separately for onshore and nononshore wind cases.

The feasibility of estimating H_s using nearshore radar echo intensities is also investigated in our study. Under higher sea states, both onshore and nononshore wind cases show similar radar echo intensities. However, the correlation between the nearshore radar echo power and *in situ* significant wave height is poor. To confirm the detailed wave features observed from radar, we also view the spectra that are estimated from sea surface images. Both the nononshore wind cases and the onshore wind cases show that the spectral shapes observed from coastal areas are scattered under gentle sea states. In addition, the spectral shapes are quite different between the onshore and nononshore wind cases. Under similar sea states, the nononshore wind cases show wider spectral shapes. Because the mechanics of radar backscattering under different environmental factors are still not fully understood, it is difficult to estimate the ocean wave spectrum accurately based on coastal radar backscattering.

After checking the influence of nononshore winds on the radar observations, we can confirm that H_s estimations can be highly uncertain in nononshore wind situations if we rely on only the linear calibration of $\sqrt{S_{\mathrm{NR}}}$ or the radar echo intensity. In this study, we attempt to consider different environmental factors and use an ANN feedforward algorithm to improve the H_s estimation. The optimization of the ANN structure is

beyond the scope of our study; hence, we implement only a simple structure for the ANN algorithm. The testing results show that we can obtain more reliable H_s estimates from both nononshore wind cases if the input parameters for the training include $\sqrt{S_{\mathrm{NR}}}$, the power from nearshore radar subimages, and *in situ* wind components. This algorithm still needs some *in situ* data to train the ANN algorithm. Some studies have proposed algorithms to estimate H_s using noncoherent radar images and do not require calibration using *in situ* data. Considering the high complexity of radar backscattering within the coastal sea area, the practicality of these calibration-free algorithms still needs to be verified for coastal radar cases.

REFERENCES

[1] M. G. Mattie and D. L. Harris, "The use of imaging radar in studying ocean waves," in *Proc. 16th Conf. Coastal Eng.*, Hamburg, Germany, Aug. 1978, pp. 174–189.

[2] I. R. Young, W. Rosenthal, and F. Ziemer, "A three-dimensional analysis of marine radar images for the determination of ocean wave directionality and surface currents," *J. Geophys. Res.*, vol. 90, no. C1, pp. 1049–1059, 1985.

[3] P. S. Bell, "Shallow water bathymetry derived from an analysis of X-band marine radar images of waves," *Coastal Eng.*, vol. 37, nos. 3–4, pp. 513–527, Aug. 1999.

[4] D. G. Long, R. S. Collyer, and D. V. Arnold, "Dependence of the normalized radar cross section of water waves on Bragg wavelength-wind speed sensitivity," *IEEE Trans. Geosci. Remote Sens.*, vol. 34, no. 3, pp. 656–666, May 1996.

[5] J. C. Nieto-Borge, P. Jarabo-Amores, D. de la Mata-Moya, and K. Hessner, "Signal-to-noise ratio analysis to estimate ocean wave heights from X-band marine radar image time series," *IET Radar, Sonar Navigat.*, vol. 2, no. 1, pp. 35–41, Feb. 2008.

[6] B. Lund, C. O. Collins, H. Tamura, and H. C. Graber, "Multi-directional wave spectra from marine X-band radar," *Ocean Dyn.*, vol. 66, no. 8, pp. 973–988, Aug. 2016.

[7] J. C. N. Borge and C. G. Soares, "Analysis of directional wave fields using X-band navigation radar," *Coastal Eng.*, vol. 40, no. 4, pp. 375–391, Jul. 2000.

[8] M. C. Haller, D. Honegger, and P. A. Catalan, "Rip current observations via marine radar," *J. Waterway, Port, Coastal, Ocean Eng.*, vol. 140, no. 2, pp. 115–124, Mar. 2014.

[9] W. Huang, X. Liu, and E. Gill, "Ocean wind and wave measurements using X-band marine radar: A comprehensive review," *Remote Sens.*, vol. 9, no. 12, p. 1261, Dec. 2017.

[10] Z. Chen, Y. He, B. Zhang, Z. Qiu, and B. Yin, "A new algorithm to retrieve wave parameters from marine X-band radar image sequences," *IEEE Trans. Geosci. Remote Sens.*, vol. 52, no. 7, pp. 4083–4091, Jul. 2014.

[11] J. An, W. Huang, and E. W. Gill, "A self-adaptive wavelet-based algorithm for wave measurement using nautical radar," *IEEE Trans. Geosci. Remote Sens.*, vol. 53, no. 1, pp. 567–577, Jan. 2015.

[12] S. Lek and Y. S. Park, "Artificial neural networks," in *Encyclopedia of Ecology*, S. E. Jørgensen and B. D. Fath, Eds. Oxford, U.K.: Academic, 2008, pp. 237–245.

[13] R. Vicen-Bueno, C. Lido-Muela, and J. C. Nieto-Borge, "Estimate of significant wave height from non-coherent marine radar images by multilayer perceptrons," *EURASIP J. Adv. Signal Process.*, vol. 2012, no. 1, p. 84, Dec. 2012.

[14] A. P. Wijaya and E. van Groesen, "Determination of the significant wave height from shadowing in synthetic radar images," *Ocean Eng.*, vol. 114, pp. 204–215, Mar. 2016.

[15] R. Gangeskar, "An algorithm for estimation of wave height from shadowing in X-band radar sea surface images," *IEEE Trans. Geosci. Remote Sens.*, vol. 52, no. 6, pp. 3373–3381, Jun. 2014.

[16] X. Liu, W. Huang, and E. W. Gill, "Wave height estimation from ship-borne X-band nautical radar images," *J. Sensors*, vol. 2016, Jun. 2015, Art. no. 1078053.

[17] W. Navarro, J. C. Velez, A. Orfila, and S. Lonin, "A shadowing mitigation approach for sea state parameters estimation using X-band remotely sensing radar data in coastal areas," *IEEE Trans. Geosci. Remote Sens.*, vol. 57, no. 9, pp. 6292–6310, Sep. 2019.

[18] G. Ludeno and F. Serafino, "Estimation of the significant wave height from marine radar images without external reference," *J. Mar. Sci. Eng.*, vol. 7, no. 12, p. 432, Nov. 2019.

[19] J. C. N. Borge, K. Reichert, and J. Dittmer, "Use of nautical radar as a wave monitoring instrument," *Coastal Eng.*, vol. 37, nos. 3–4, pp. 331–342, Aug. 1999.

[20] B. Lund, C. O. Collins, H. C. Graber, E. Terrill, and T. H. C. Herbers, "Marine radar ocean wave retrieval's dependency on range and azimuth," *Ocean Dyn.*, vol. 64, no. 7, pp. 999–1018, Jul. 2014.

[21] D.-J. Doong, L.-C. Wu, and J.-W. Lai, "Determination of the spatial pattern of wave directions in the inhomogeneous coastal ocean by marine radar image sequences," *IEEE Access*, vol. 6, pp. 45762–45771, 2018.

[22] K. Hessner, K. Reichert, and J. Dannenberg, "2-D surface elevation measurements by means of X-band radar: An application of WAMOS II at duck," in *Proc. 9th Int. Workshop Wave Hindcasting Forecasting*, Victoria, BC, Canada, 2006, pp. 1–13.

[23] Y. Liu, W. Huang, and E. W. Gill, "Analysis of the effects of rain on surface wind retrieval from X-band marine radar images," in *Proc. Oceans*, Sep. 2014, pp. 1–4.

[24] J. C. Daley, "Wind dependence of radar sea return," *J. Geophys. Res.*, vol. 78, no. 33, pp. 7823–7833, Nov. 1973.

[25] J. E. Simpson, *Sea Breeze and Local Winds*. Cambridge, U.K.: Cambridge Univ. Press, 1994.

[26] W. J. Plant, W. C. Keller, K. Hayes, and G. Chatham, "Normalized radar cross section of the sea for backscatter: 1. Mean levels," *J. Geophys. Res.*, vol. 115, no. C9, 2010, Art. no. C09032.

[27] M. B. Kanevsky, *Radar Imaging of the Ocean Waves*. Amsterdam, The Netherlands: Elsevier, 2008.

[28] O. Gronlie, "Wave radars: A comparison of concepts and techniques," *Hydro Int.*, vol. 8, pp. 24–27, Jun. 2004.

[29] J. Nieto-Borge, M.-P. Jarabo-Amores, D. al, and F. López-Ferreras, "Estimation of ocean wave heights from temporal sequences of X-band marine radar images," in *Proc. 14th Eur. Signal Process. Conf.*, 2006, pp. 1–5.

[30] G. Ludeno *et al.*, "Remocean system for the detection of the reflected waves from the costa concordia ship wreck," *IEEE J. Sel. Topics Appl. Earth Observ. Remote Sens.*, vol. 7, no. 7, pp. 3011–3018, Jul. 2014.

[31] R. Gangeskar, "Ocean current estimated from X-band radar sea surface, images," *IEEE Trans. Geosci. Remote Sens.*, vol. 40, no. 4, pp. 783–792, Apr. 2002.

[32] L. Cornejo-Bueno, J. C. N. Borge, E. Alexandre, K. Hessner, and S. Salcedo-Sanz, "Accurate estimation of significant wave height with support vector regression algorithms and marine radar images," *Coastal Eng.*, vol. 114, pp. 233–243, Aug. 2016.

[33] G. Ludeno *et al.*, "Normalized scalar product approach for nearshore bathymetric estimation from X-band radar images: An assessment based on simulated and measured data," *IEEE J. Ocean. Eng.*, vol. 43, no. 1, pp. 221–237, Oct. 2017.

[34] P. S. Bell and J. C. Osler, "Mapping bathymetry using X-band marine radar data recorded from a moving vessel," *Ocean Dyn.*, vol. 61, no. 12, pp. 2141–2156, Dec. 2011.

[35] K. Hessner, S. Wallbridge, and T. Dolphin, "Validation of areal wave and current measurements based on X-band radar," in *Proc. IEEE/OES 11th Current, Waves Turbulence Meas. (CWTM)*, Mar. 2015, pp. 1–10.

[36] Y. Goda, "A comparative review on the functional forms of directional wave spectrum," *Coastal Eng. J.*, vol. 41, no. 1, pp. 1–20, Mar. 1999.

[37] J. P. Vandever, E. M. Siegel, J. M. Brubaker, and C. T. Friedrichs, "Influence of spectral width on wave height parameter estimates in coastal environments," *J. Waterway, Port, Coastal, Ocean Eng.*, vol. 134, no. 3, pp. 187–194, May 2008.

[38] Y. Goda, *Random Seas and Design of Maritime Structures*, 2nd ed. Singapore: World Scientific, 2000.

[39] H. Dankert and J. Horstmann, "A marine radar wind sensor," *J. Atmos. Ocean. Technol.*, vol. 24, no. 9, pp. 1629–1642, Sep. 2007.

[40] L. H. Holthuijsen, *Waves in Oceanic And Coastal Waters*. Cambridge, U.K.: Cambridge Univ. Press, 2007.

[41] G. Zhang, B. E. Patuwo, and M. Y. Hu, "Forecasting with artificial neural networks: The state of the art," *Int. J. Forecasting*, vol. 14, no. 1, pp. 35–62, 1998.

Li-Chung Wu received the Ph.D. degree in engineering from National Cheng Kung University, Tainan, Taiwan, in 2008.

He has been an Associate Research Fellow with the Coastal Ocean Monitoring Center, National Cheng Kung University, since 2019. His research interests include remote sensing, ocean engineering, image processing, and wavelet transform.

Dong-Jiing Doong received the Ph.D. degree from National Cheng Kung University (NCKU), Tainan, Taiwan, in 2002.

He is a Professor with the Department of Hydraulic and Ocean Engineering, NCKU. His research interests include remote sensing techniques, ocean waves, and coastal hazards and protection.

Jian-Wu Lai received the Ph.D. degree in engineering from National Cheng Kung University, Tainan, Taiwan, in 2009.

He has been a Research Fellow with the Marine Industry and Engineering Research Center, National Academy of Marine Research, Kaohsiung, Taiwan, since 2019. His research interests include marine hydrodynamics and coastal process, remote sensing, and coastal disaster strategies.